

Dimensionality reduction and dynamical filtering: Stimulated Brillouin scattering in optical fibersRafael G. Setra,^{1,2} Diana A. Arroyo-Almanza,^{1,3} Zetian Ni,^{1,4,5} Thomas E. Murphy,^{1,2} and Rajarshi Roy^{1,3,4}¹*Institute for Research in Electronics and Applied Physics, University of Maryland, College Park, Maryland 20742, USA*²*Department of Electrical and Computer Engineering, University of Maryland, College Park, Maryland 20742, USA*³*Institute for Physical Science and Technology, University of Maryland, College Park, Maryland 20742, USA*⁴*Department of Physics, University of Maryland, College Park, Maryland 20742, USA*⁵*Department of Physics, Shanghai Jiao Tong University, Shanghai 200240, China*

(Received 9 March 2015; published 4 August 2015)

Stimulated Brillouin scattering (SBS) is a noise-driven nonlinear interaction between acoustical and optical waves. In optical fibers, SBS can be observed at relatively low optical powers and can severely limit signal transmission. Although SBS is initiated by high dimensional noise, it also exhibits many of the hallmarks of a complex nonlinear dynamical system. We report here a comprehensive experimental and numerical study of the fluctuations in the reflected Stokes wave produced by SBS in optical fibers. Using time series analysis, we demonstrate a reduction of dimensionality and dynamical filtering of the Stokes wave. We begin with a careful comparison of the measured average transmitted and reflected intensities from below the SBS threshold to saturation of the transmitted power. Initially the power spectra and correlation functions of the time series of the reflected wave fluctuations at the SBS threshold and above are measured and simulated. Much greater dynamical insight is provided when we study the scaling behavior of the intensity fluctuations using Hurst exponents and detrended fluctuation analysis for time scales extending over six orders of magnitude. At the highest input powers, we notice the emergence of three distinct dynamical scaling regimes: persistent, Brownian, and antipersistent. Next, we explore the Hilbert phase fluctuations of the intensity time series and amplitude-phase coupling. Finally, time-delay embedding techniques reveal a gradual reduction in dimensionality of the spatiotemporal dynamics as the laser input is increased toward saturation of the transmitted power. Through all of these techniques, we find a transition from noisier to smoother dynamics with increasing input power. We find excellent agreement between our experimental measurements and simulations.

DOI: [10.1103/PhysRevE.92.022903](https://doi.org/10.1103/PhysRevE.92.022903)

PACS number(s): 05.45.–a, 42.70.Ce

I. INTRODUCTION

Brillouin scattering is a well-known effect in which a photon is inelastically scattered or reflected by a density fluctuation or acoustical phonon in a material. At sufficiently high optical power, the optical field in turn produces a mechanical strain through the process of electrostriction, which is the origin of the nonlinear effect termed stimulated Brillouin scattering (SBS) [1–3]. While SBS can be described as a nonlinear interaction among two counterpropagating optical waves and an acoustical wave, it can emerge from a single optical input wave in the presence of thermal acoustical fluctuations. SBS is one of the leading nonlinear impairments in fiber optic communication and high-powered laser systems, where it can produce a strong, fluctuating backward-propagating Stokes wave even at relatively low optical input power [4,5]. An existing method to control SBS is through modulation of the input laser [6,7]. Additionally, SBS is also seen in plasmas [8–11], where it produces deleterious effects in the laser-plasma interaction necessary for inertial confinement fusion. Although SBS can result in severe impairments in laser communications, it is also a flexible mechanism for controlling light. In particular, there has been interest in using SBS for integrated circuits, which is possible by tailoring wave guides to produce SBS with large gains [12–16]. Recently SBS has also been characterized in media such as perfluorocarbon-compounds [17], where SBS behaves stably for high-input powers needed for high-power laser systems, and in photonic crystal fibers, where the tight confinement of light allows a strong photon-phonon interaction, which

is excellent for exploiting SBS [18]. Existing applications of SBS are numerous, including microwave generation [19], self-induced transparency [20], large controlled delays for subnanosecond pulses [21], optical spectrum analysis [22], and storing light [23]. The interest of SBS ranges from removing the detrimental effects in fiber optic communication and high-power laser systems to exploiting it as a key process for optical control and information processing. In all of these cases, understanding and characterizing the dynamics of noise-driven SBS allow for improved exploitation of its effects in many applications.

Since the early observations of SBS, powerful new techniques have been developed for acquiring and quantifying the nature of fluctuations in time series. Surprisingly, these techniques have yet to be applied to study how the stochastic fluctuations observed at the onset of SBS evolve into emergent dynamical states as the optical power is increased. In this work we observe and analyze the dynamics of SBS in single-mode optical fiber without external feedback as a function of the input power. We find that a transition from high-dimensional noisy dynamics to smoother lower dimensional dynamics occurs as the input power increases above the threshold for SBS. The interpretation of this transition as being due to dynamical filtering and spectral reshaping is supported quantitatively by the results of multiple time series analysis techniques.

Although SBS is initiated and sustained by noise [24,25], the resulting optical and acoustical fluctuations can grow to macroscopic amplitudes that far exceed the thermal inhomogeneities from which they originate. In this regime,

the signals acquire the distinct dynamical signature of the nonlinear governing equations. While the process originates in thermal noise, the emerging signals at higher input powers are quite distinct due to the nonlinear spatiotemporal equations governing the system. Nature is filled with examples of noise-initiated and influenced complex dynamical phenomena. Models of the emergence and spread of viral epidemics [26] and ecological models of species populations and natural resources often require stochastic noise sources to account for observations made in the field [27–29]. Unlike most systems found in nature, stimulated Brillouin scattering is a rare example of a spatiotemporal noise-driven system with very accessible data.

Recent studies of chaotic lasers and random number generation have suggested that spontaneous emission fluctuations are amplified to observable macroscopic signals by chaotic dynamics [30]. In these examples, complex macroscopic dynamical states emerge from small stochastic fluctuations. Understanding and predicting the behavior of such systems requires a clear understanding of the interplay between noise and dynamics. In the case of SBS, Gaeta and Boyd showed that the intensity fluctuations were stochastic near the threshold of initiation [1]. The fluctuations can also behave chaotically as predicted theoretically by Randall [31] and shown experimentally by Harrison *et al.* [32,33] and Lee *et al.* [34], in the presence of external feedback. In the studies presented here, we examine fluctuations of the reflected Stokes wave with negligible external feedback and determine the scaling properties and exponents as well as determine the dimensionality of the phase-space dynamics by time-delay reconstruction.

II. SPATIOTEMPORAL MODEL AND EXPERIMENTAL APPARATUS

The Brillouin scattering process may be described by three complex coupled partial differential equations [1–3,35,36]:

$$\frac{\partial E_L}{\partial z} + \frac{n}{c} \frac{\partial E_L}{\partial t} = -\frac{\alpha}{2} E_L + i\kappa E_S \rho, \quad (1a)$$

$$-\frac{\partial E_S}{\partial z} + \frac{n}{c} \frac{\partial E_S}{\partial t} = -\frac{\alpha}{2} E_S + i\kappa E_L \rho^*, \quad (1b)$$

$$\frac{\partial \rho}{\partial t} + \pi \Delta \nu_B \rho = i\Lambda E_L E_S^* + f(z,t). \quad (1c)$$

The input laser electric field $E_L(z,t)$, the backward Stokes wave electric field $E_S(z,t)$, and the density variation $\rho(z,t)$ from its mean ρ_0 are functions of time t and position z within the fiber. The spectral full-width-at-half-maximum Brillouin line width is $\Delta \nu_B \approx 35$ MHz. The fiber attenuation coefficient α is 0.209 dB/km for our optical fiber with index of refraction $n = 1.45$ and c the speed of sound in a vacuum.

The coupling parameter κ is expressed as

$$\kappa = \frac{\pi \gamma}{2n\rho_0 \lambda_L M} \quad (2)$$

with electrostriction coefficient $\gamma = 0.902$ 1/(Wm) [37] and a mean density $\rho_0 = 2210$ kg/m³. The polarization is assumed to be completely scrambled so that the polarization parameter $M = 1.5$ [38]. In our experiments we used an incident laser wavelength of $\lambda_L = 1550$ nm. The acoustic coupling

parameter [36] is

$$\Lambda = \frac{\pi n \epsilon_0 \gamma}{\lambda_L v}, \quad (3)$$

where ϵ_0 is the permittivity of free space and the speed of sound v is 5800 m/s. The Langevin noise source $f(z,t)$, arising from thermal phonons, is delta-correlated in time and space so that $\langle f(z,t) f^*(z',t') \rangle = Q \delta(z - z') \delta(t - t')$ [24]. The noise source strength is described by

$$Q = \frac{4\pi k T \rho_0 \Delta \nu_B}{v^2 A} \quad (4)$$

with Boltzmann's constant k , a room temperature of $T = 293$ K, and fiber modal area A of $55 \mu\text{m}^2$.

The boundary conditions for the transmitted and Stokes waves are $E_S(L,t) = 0$, $E_S(z,0) = 0$, and $E_L(0,t) = [(2P_{\text{in}})/(nc\epsilon_0 A)]^{\frac{1}{2}}$ where P_{in} is the laser input power. Here $L = 12.6$ km is the length of the fiber. The boundary conditions for the density variation are

$$\rho(z,0) = \sqrt{\frac{nQ}{2c\pi \Delta \nu_B}} S(z,0), \quad (5a)$$

$$\rho(0,t) = \sqrt{\frac{nQ}{2c\pi \Delta \nu_B}} S(0,t), \quad (5b)$$

where $S(0,t)$ and $S(z,0)$ are complex Gaussian random variables with zero mean and unit variance [35]. The equations are solved by an iterative Euler finite-difference method with appropriately chosen step sizes of $dt = 2$ ns and $dz = (c/n)dt$ to ensure numerical accuracy. The equations are first integrated up to $t = 20t_f$, where t_f is the transit time (nL/c), to remove initial transients and then integrated for an additional 40 transit times to provide our simulated data. This model is flexible and may be altered to account for initial laser phase modulation [36] and even transients in stimulated Brillouin scattering pulse compressors [39].

The experimental setup used to examine SBS is shown in Fig. 1. The light from the tunable laser (Agilent 81682A) is amplified by a high-power erbium-doped fiber amplifier. The signal is then passed through an optical variable attenuator before it enters into the optical fiber. Afterwards the light is launched into a 12.6-km single-mode fiber by an optical circulator. This directs the Stokes light into a photoreceiver, which is then displayed on a digital oscilloscope (Tektronix

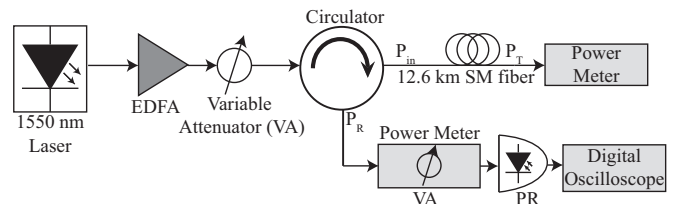


FIG. 1. Experimental setup for SBS measurements. An erbium-doped fiber amplifier (EDFA) and variable attenuator (VA) are used to control the input power P_{in} before entering the single-mode (SM) optical fiber. The circulator redirects the reflected wave onto another VA before a photoreceiver (PR) converts the light into an electrical signal to be collected by a digital oscilloscope.

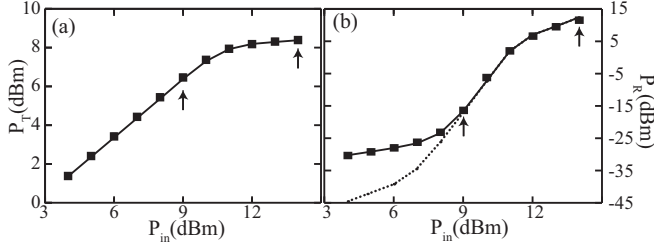


FIG. 2. Measured transmitted power P_T (a) and reflected power P_R (b) vs P_{in} . Dark squares are experimental measurements; smooth lines are simulated timed-averaged power values. The dotted line in (b) is the simulation without Rayleigh backscattering.

DPO 4034B) with a 250 MHz sampling frequency; the oscilloscope bandwidth is 350 MHz. In our experiments we use angled optical fiber connectors for the laser input and output and find no trace of external feedback, periodicity [40], or chaos [41].

III. OVERVIEW OF SBS

The measured transmitted and reflected output powers are plotted in Figs. 2(a) and 2(b) alongside the simulated powers obtained from Eqs. (1a)–(1c) calculated by time averaging the simulated transmitted and reflected optical fields:

$$P_T = \frac{nc\epsilon_0 A}{2} \langle |E_L(L, t)|^2 \rangle, \quad (6a)$$

$$P_R = \frac{nc\epsilon_0 A}{2} \langle |E_S(0, t)|^2 \rangle. \quad (6b)$$

In Fig. 2(b) we see that the backward wave grows rapidly with increasing input power, and SBS eventually depletes most of the light from the transmitted beam. Simulated and experimental data are in good agreement after accounting for Rayleigh scattering [36] in the reflected power through an additive term of $3.3 \times 10^{-4} P_{in}$. Similar effects on the reflected and transmitted output powers in plasma can also be seen at various wavelengths [42]. SBS is a severe impairment in laser communications because of this rapid rise in reflected power and saturation of transmitted power.

We will examine in detail the time series of the Stokes wave at input powers of 9 dBm and 14 dBm, which are indicated by the arrows in Figs. 2(a) and 2(b); at P_{in} of 9 dBm we are near the onset of SBS where the reflected output power is relatively weak compared to the transmitted power, and at 14 dBm the transmitted power approaches saturation. To compare simulated and experimental time series, the simulated wave is sampled at 4 ns and passed through a high-pass filter with a cut-on of 30 kHz to match that of the photoreceiver. Finally, the background noise measured from the photoreceiver, scaled with respect to amplitude, is added to the simulated data.

In Fig. 3 are the resulting temporal fluctuations of the Stokes intensity I_s , normalized with respect to its standard deviation σ_s ; we present a detailed statistical and nonlinear analysis in the following sections, which shows good agreement between simulation and experiment. Also, we confirmed that these fluctuations follow an exponential distribution in agreement with previous observations [43].

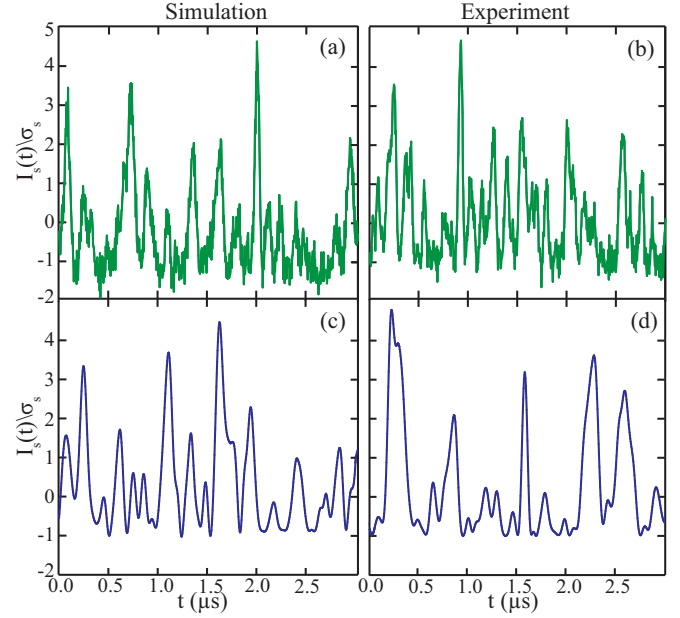


FIG. 3. (Color online) Time series, sampled at 4 ns intervals, of the Stokes wave intensity $I_s(t)$ normalized to the standard deviations σ_s from input powers of 9 dBm (a) simulation; (b) experiment, and 14 dBm (c) simulation; (d) experiment.

IV. RESULTS AND DISCUSSION

A. Intensity correlations and power spectra

In Fig. 4 are shown the intensity autocorrelation functions for input powers of 9 dBm and 14 dBm. The correlation functions are characterized by peaks of width approximately 50 ns followed by a small tail which continues for larger time scales not shown in Fig. 4. Although the reflected powers between 9 dBm and 14 dBm inputs change by a factor of nearly 1000, the fluctuation time scales of the intensity correlations are not that different. The constancy in fluctuation time scales has also been observed by Gaeta and Boyd [1].

Shown in Fig. 5 are the power spectra of the simulated Stokes wave intensity fluctuations. These simulations have not been calibrated to the experimental setup so that we may see the Stokes spectrum for very low input powers. For the lowest input power of 4 dBm in Fig. 5(a) there is a significant

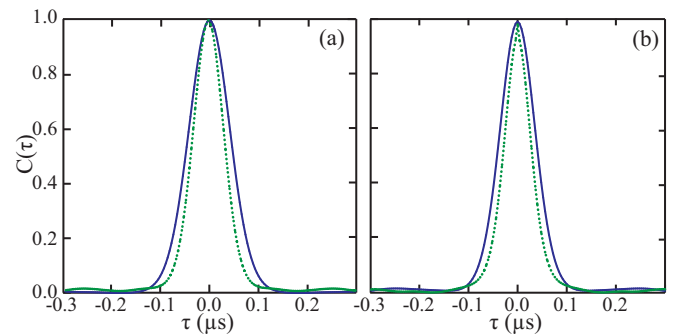


FIG. 4. (Color online) Normalized intensity autocorrelation functions $C(\tau)$ of simulations (a) and experimental measurements (b) of reflected waves from input powers of 9 dBm (green dotted line) and 14 dBm (solid blue line).

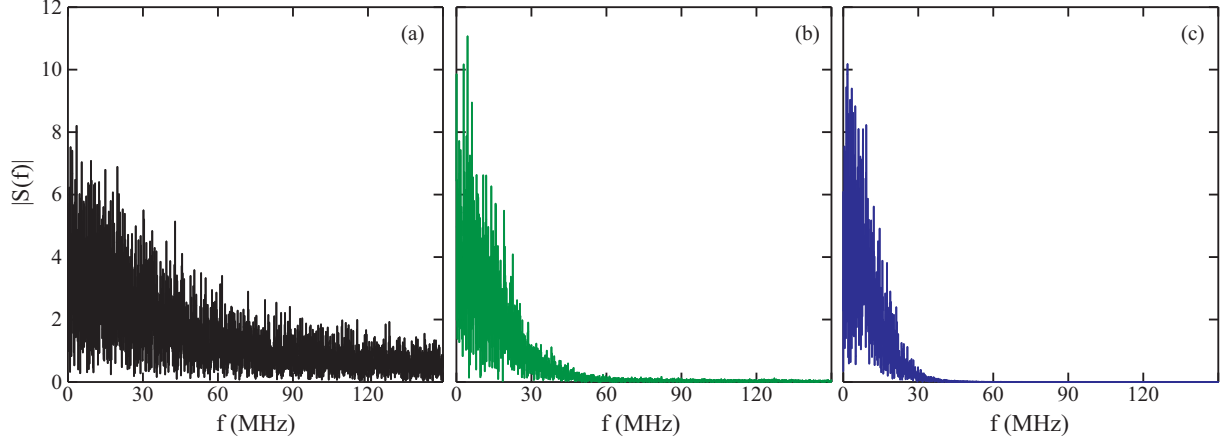


FIG. 5. (Color online) Stokes power spectrum $|S(f)|$, calculated by normalizing the fast Fourier transform of zero-mean simulated intensity fluctuations to its standard deviation. Plots shown are for input powers of 4 dBm black (a), 9 dBm green (b), and 14 dBm blue (c).

amount of power at frequencies above the Brillouin line width of 35 MHz. As the input power is increased, not only does the line width of the spectrum begin to narrow, but the large tail additionally decreases in magnitude through the dynamical filtering of system. This change may be quantified by the root-mean-square bandwidth calculated using

$$\sigma_B = \sqrt{\frac{\int_0^{f_u} f^2 |S(f)| df}{\int_0^{f_u} |S(f)| df}}. \quad (7)$$

Here $|S(f)|$ is the Stokes power spectrum from Fig. 5, and we take the upper limit f_u to be 150 MHz. The root-mean-squared bandwidth changes from 61.08 MHz at the lowest input power of 4 dBm, to 26.10 MHz for 9 dBm, and finally to 8.51 MHz for 14 dBm; there is clear narrowing. The line-width narrowing found in our intensity fluctuations is similar to those seen in the direct measurements of the optical spectrum by Gaeta and Boyd [1]. Finally, in Fig. 6 we create a direct comparison between the power spectra of the experimental and simulated intensity fluctuations by compensating for the photoreceiver filter and photoreceiver noise in our experimental setup. We see excellent agreement between simulated and experimental power spectra, both of which display line width narrowing and tail reduction with increasing input power. The spectral reshaping between the two input powers indicates a transition from high-dimensional noise towards a lower-dimensional system as will be demonstrated in Sec. IV D.

B. Scaling behavior

As shown in Figs. 4(a) and 4(b), the intensity correlation functions and timescales are similar for both low and high input powers; however, further examination of the scaling behavior shows a dramatic difference. One way to quantify long-term dependence is through the Hurst exponent H , first used to study optimal dam sizing [44]. A method of estimating this exponent is through detrended fluctuation analysis (DFA) which was first used on DNA sequences [45] and may also be used on systems with time-varying Hurst exponents [46]. Processing a time series $X(n)$ of length N through the DFA consists of

several steps. The first is subtracting the mean \bar{X} from the data and creating a cumulative sum:

$$Y(n) = \sum_{i=1}^n [X(i) - \bar{X}]. \quad (8)$$

This cumulative sum is then separated into different data sets of window length ΔT . Each of these sets is detrended within the window by a polynomial of known order; in our case a linear fit is adequate. The fluctuations are then calculated as the root-mean squared deviation of $Y(n)$ from the piecewise linearly approximated series $Y_{\Delta T}^{(1)}(n)$:

$$F(\Delta T) = \left\{ \frac{1}{N} \sum_{i=1}^N [Y(i) - Y_{\Delta T}^{(1)}(i)]^2 \right\}^{\frac{1}{2}}. \quad (9)$$

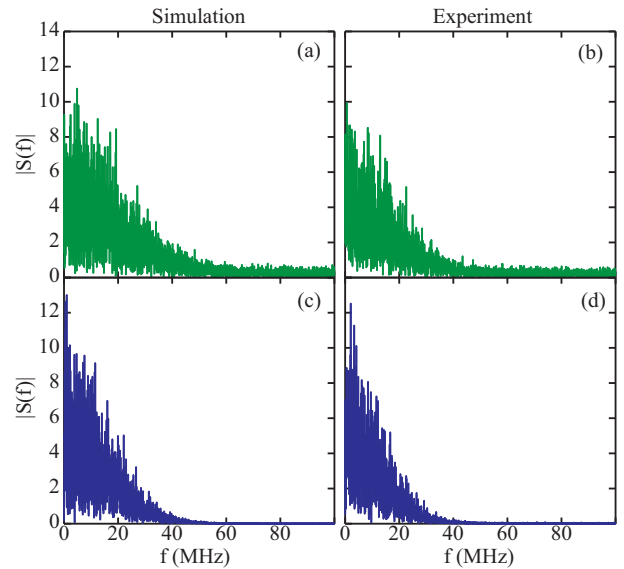


FIG. 6. (Color online) Stokes power spectrum $|S(f)|$, calculated by normalizing the fast Fourier transform of intensity fluctuations in Fig. 3 to its standard deviation. Plots shown are for input powers of 9 dBm (a) simulation; (b) experiment, and 14 dBm (c) simulation; (d) experiment.

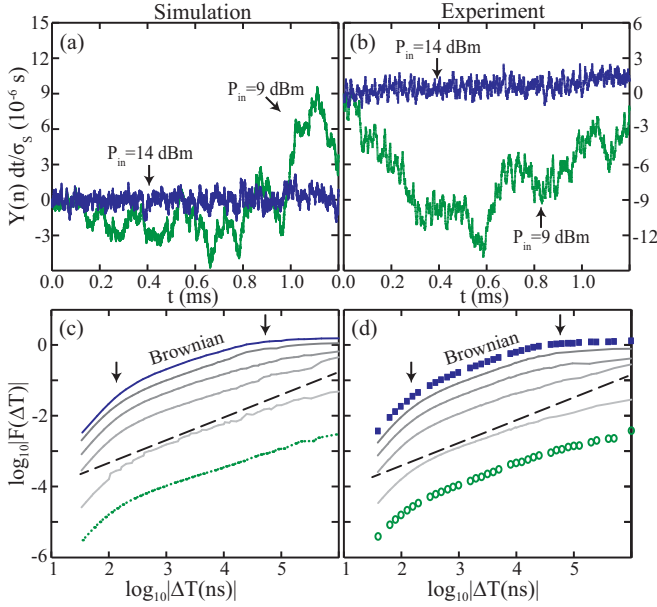


FIG. 7. (Color online) Normalized integral of the intensity time series of Fig. 3 for simulated (a) and experimental (b) data for P_{in} of 9 dBm (green) and 14 dBm (blue): $Y(n) = \sum_{i=1}^n I_s(i)$. Fluctuations of Stokes wave intensities for simulated (c) and experimental (d) data for 9 dBm (green dotted line, simulation; green circle, experiment) and 14 dBm [blue solid (highest) line, simulation; blue square, experiment]. The remaining gray solid lines represent fluctuations of Stokes wave intensities for input powers of 10 (lightest gray, second lowest), 11, 12, and 13 dBm (darkest gray, second highest). The dashed black line has a slope of 0.5 (Brownian motion). The arrows indicate crossover points between persistent, Brownian, and antipersistent scaling regimes.

We study the power-law scaling behavior $F(\Delta T) \sim (\Delta T)^\alpha$ of the fluctuations from the Stokes waves to approximate H . We have that $H = \alpha$ for fractional Gaussian noise (fGn) and $H + 1 = \alpha$ for fractional Brownian motion (fBm) because fBm is the cumulative sum or integral of fGn. Shown in Figs. 7(a) and 7(b) are the integrals of the zero-mean and normalized Stokes waves from input powers of 9 dBm and 14 dBm. The time scale here is much larger than the correlation widths in Fig. 3, and clear differences are now evident. At the lower power the integral drifts over a wide range, while at the higher power the drift is significantly limited. By applying the DFA to the fluctuations of the actual signals, we can clearly quantify the difference. A plot of the fluctuations against window length is shown in Figs. 7(c) and 7(d). Since we have not normalized the time series for Figs. 7(c) and 7(d) we can first notice that the curves from input powers of 9 dBm and 14 dBm are offset by about 3 orders of magnitude, corresponding to the 30 dB difference in reflected power. Furthermore, several regions have different scaling behaviors. First, before a crossover point on the order of the correlation time of roughly 50 ns, indicated by the first arrow, the intensity fluctuations due to P_{in} of 14 dBm have a steep slope of $\alpha = 1.75$, which is indicative of persistent data with a Hurst exponent $H = 0.75$. In the 9 dBm case these slopes are 1.79 with $H = 0.79$. These large Hurst exponents correspond to the small time scale under which the integrated curves appear

fairly smooth. After the crossover point the slopes in the 14 dBm and 9 dBm cases are 0.55 and 0.56, respectively, which means the integrated curves in this window length are similar to Brownian motion with $H = 0.5$ [47]. This scaling behavior resembling randomness is a property of the noise initiation of SBS. The scaling exponents are similar for both low and high input powers on these window lengths, but the exponents change significantly for larger window lengths. For window lengths above the fiber transit time ($\approx 60 \mu\text{s}$), indicated by the second arrow, the slope decreases to 0.08 for the 14 dBm case, evidence of antipersistent fluctuations. This is a clear transition from the slope of 0.46 for the 9 dBm case. Intermediate values are slopes of 0.47, 0.41, 0.29, and 0.07 for input powers of 10, 11, 12, and 13 dBm respectively, which show a gradual transition from Brownian motion dynamics towards an antipersistent system. This behavior is very visible from the integrals plotted in Fig. 7(a) and 7(b). While the original temporal fluctuations of the Stokes wave resemble an exponential distribution, which has the “memoryless” property [48], the integrals of these waves transition from dominantly Brownian motion statistics to an antipersistent behavior with memory. The transition occurs as the input power is increased to a level where the transmitted power saturates and the nonlinear dynamics governing SBS evolution becomes significant. This memory originates from the Stokes wave affecting the input laser at the front end of the fiber. The modified pump wave carries information from the Stokes wave and alters the Stokes wave dynamics at the end of the fiber, effectively impressing the history of the previous Stokes wave.

C. Hilbert phase analysis

The intensity dynamics of the Stokes wave due to low and high input powers behave very differently over long time scales, and it is interesting to ask if a change in dynamics also occurs for the phase fluctuations. In a previous study, the phase of Stokes pulses in gases were observed to have large phase jumps [25], but here we study the phase of a continuous wave laser in an optical fiber and we find a transition away from noiselike behavior. Since we do not have optical phases for the experimental measurements, we can use the residual Hilbert phase increments of the unwrapped Hilbert phase calculated from the analytic signal $X_a(n) = X(n) + i\hat{X}(n)$, where $\hat{X}(n)$ is the Hilbert transform of $X(n)$ [49,50].

Calculating the residual phase increments of a time series $X(n)$ consists of several steps. The first is to obtain the analytic signal $X_a(n) = X(n) + i\hat{X}(n)$, where $\hat{X}(n)$ is the Hilbert transform of $X(n)$. From this complex signal we create the unwrapped version of the Hilbert phase obtained from the four-quadrant inverse tangent function. The unwrapped Hilbert phases when $X(n)$ is the Stokes wave time series for input powers of 9 dBm and 14 dBm are shown in Figs. 8(a), 8(c), 8(e), and 8(g) with respective zooms displayed in Figs. 8(b), 8(d), 8(f), and 8(h).

We then approximate this unwrapped phase with a line of best fit, as shown in Figs. 8(b), 8(d), 8(f), and 8(h), and produce the residuals by subtracting the best-fit line from the unwrapped phase. These Hilbert phase residuals obtained from the Stokes wave for input powers of 9 dBm and 14 dBm are shown in Figs. 9(a), 9(c), 9(e), and 9(g) respectively.

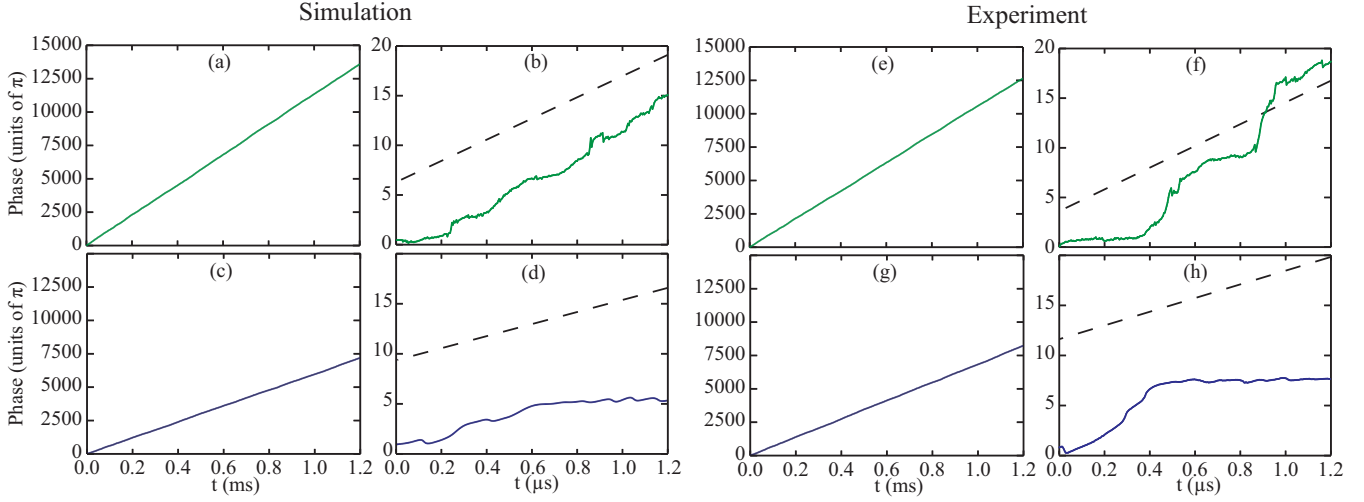


FIG. 8. (Color online) Unwrapped Hilbert phase from time series $X(n)$ of the simulated backward Stokes wave obtained from input powers of 9 dBm (a) with zoom (b) and 14 dBm (c) with zoom (d). Solid lines are the phases plotted at 4 ns intervals for 300 000 points (a), (c) and 300 points (b), (d). Dashed lines are best fit lines of the unwrapped Hilbert phase for 1.2 ms (a), (c). Corresponding measurements for experimental data are in (e)–(h).

We observe that for both low and high input powers the phases appear to be drifting randomly. Finally, shown in Figs. 9(b), 9(d), 9(f), and 9(h) are zoomed-in versions of Figs. 9(a), 9(c), 9(e), and 9(g). In these zooms of the phase residuals we can see noisy characteristics found in the lower input powers. In addition, the arrows indicate examples of large jumps in phase above $\pi/2$.

In Figs. 10(a)–10(d) we display the analytic signal magnitude and phase in polar coordinates for a short time interval of $2 \mu s$. For an input power of 9 dBm there is evidence of a sharply fluctuating trajectory. For the 14 dBm case the trajectories in the polar graphs are much smoother. This may be accounted for by the relative decrease in large phase jumps as input power increases. Plotted in Fig. 11 are the number of phase jumps larger than $\pi/2$ for various input powers, calculated through the discretized derivative of the residual

phase. We note that similar large phase jumps, manifestations of the noise which initiates SBS, were first revealed through heterodyne measurements in Ref. [25]. The movement from a high-dimensional noisy behavior to a lower-dimensional system seen in these polar plots is due to the decrease in the number of large phase jumps as we increase the input, and thus the reflected power, to a level far beyond the strength of the noise which initiates SBS.

D. Time-delay embedding and dimensionality reduction by dynamical filtering

The last method to characterize the transition in dynamical behavior is through estimating the dimensionality of the phase space needed to capture the dynamics of the Stokes waves. In Figs. 12(a) and 12(b) are time-delay embeddings of the

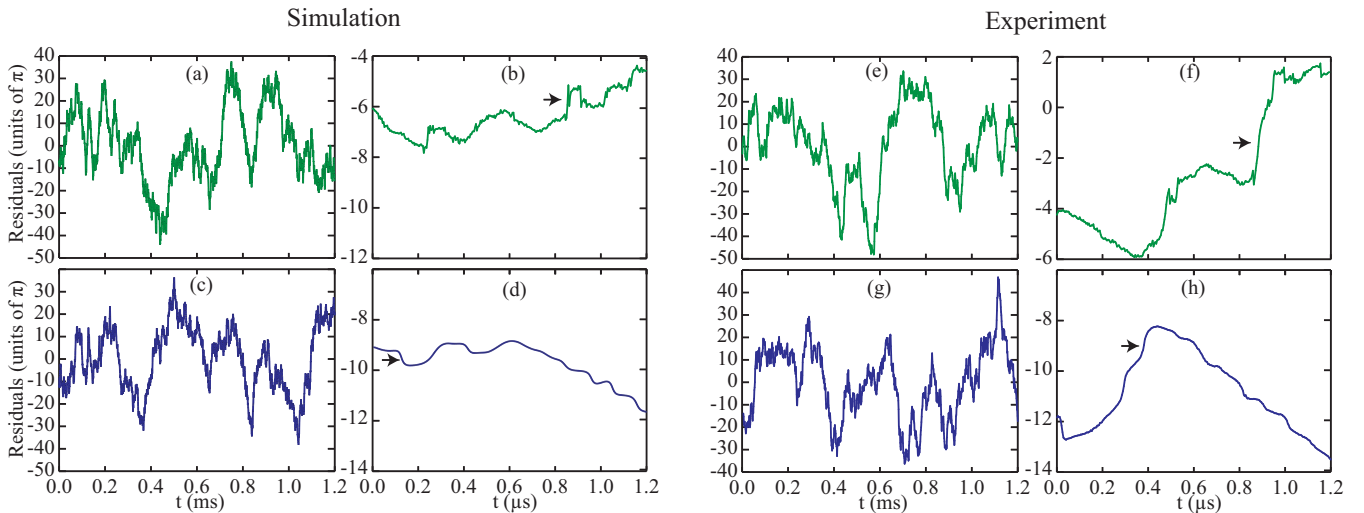


FIG. 9. (Color online) Hilbert phase residuals from time series $X(n)$ of the simulated backward Stokes wave obtained from input powers of 9 dBm (a) with zoom (b) and 14 dBm (c) with zoom (d). Arrows indicate examples of phase jumps above $\pi/2$. Corresponding measurements for experimental data are in (e)–(h).

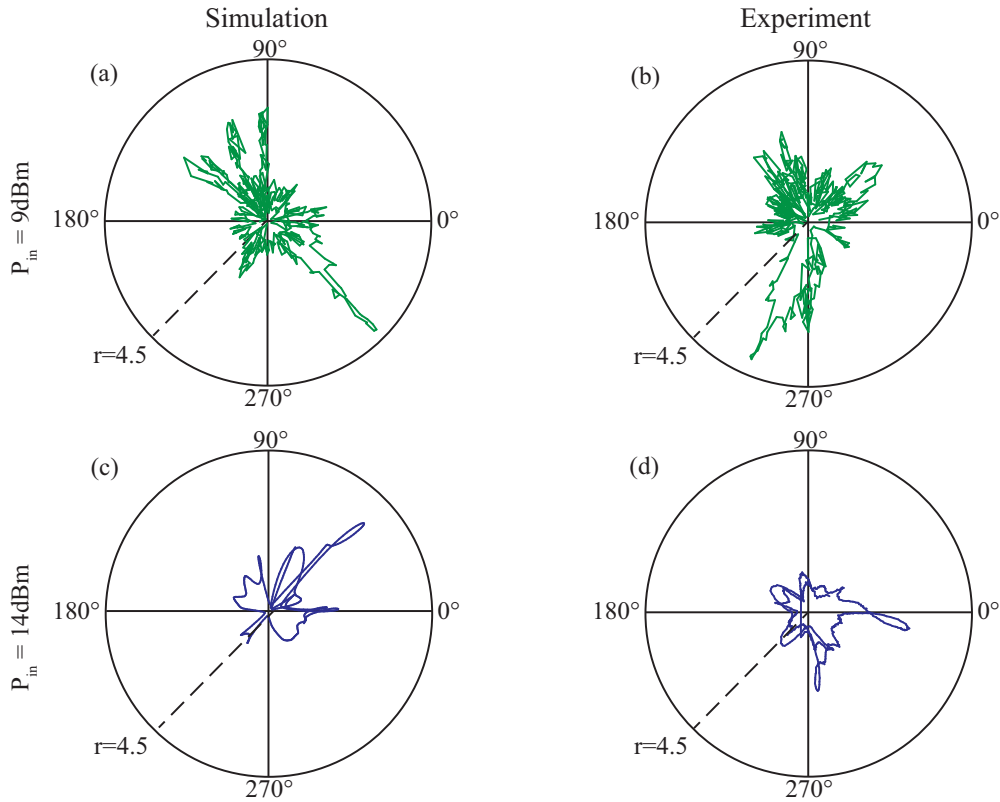


FIG. 10. (Color online) Polar plots of 500 points at 4 ns intervals of the analytic signal magnitude and residual phase generated by the Stokes wave with P_{in} of 9 dBm (a) simulation; (b) experiment, and 14 dBm (c) simulation; (d) experiment.

measured Stokes intensities from input powers of 9 dBm and 14 dBm for a time interval of 6 μs . In these two-dimensional embeddings the lower input power again results in a noisier less coherent form than the higher power. However, a dimension of two is not enough to capture the Stokes wave dynamics.

An algorithm for finding the minimum embedding dimension of a time series is the false nearest neighbors algorithm [51]. Nearest neighbors are identified in the phase space within a threshold distance but may no longer be nearest neighbors when embedded into a higher dimension. The percentage of these false nearest neighbors is then calculated for chosen embedding dimensions. A sophisticated variant is the false nearest strands (FNS) algorithm [52], which groups adjacent neighbors into a strand to remove some correlation,

and nearest strands are then compared for increasing embedding dimensions. In Fig. 13(a) we apply the FNS algorithm to simulated Stokes waves for input powers of 4, 7, 9, and 14 dBm. For the 4 dBm case the amount of false nearest strands does not vanish with increasing dimension, which is a typical signature of noisy dynamics. With increasing input power, the percentage of nearest strands steadily decreases and converges towards zero at an embedding dimension of eight. As in Fig. 3, to directly compare the experimental data to simulations we apply a high-pass filter and additive noise to the simulated data and plot the results of the FNS algorithm in Fig. 13(b). For comparison we plot the percentage of FNS for the measured noise. We conclude from the excellent comparison between experimental and simulated data that

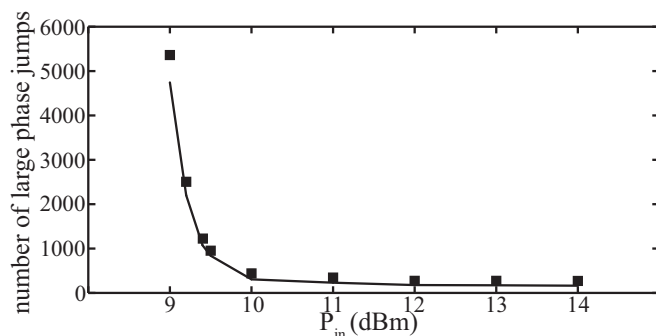


FIG. 11. Count of phase jumps larger than $\pi/2$ for simulated (solid line) and experimental (square) time series of 300 000 points.

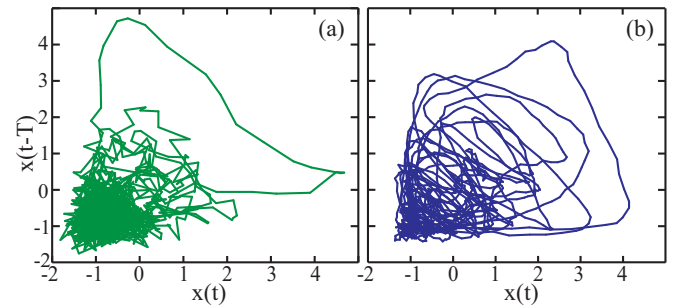


FIG. 12. (Color online) Time-delay embeddings of experimental Stokes wave time series for input powers of 9 dBm (a) and 14 dBm (b) from 1500 points at 4 ns intervals. We selected delays T of 52 ns (a) and 48 ns (b) from the data in Fig. 3(f).

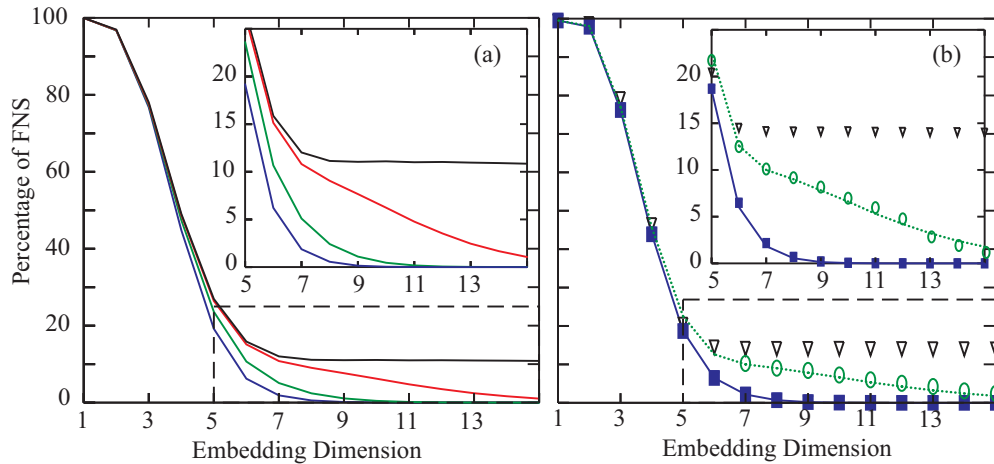


FIG. 13. (Color online) Percentage of false nearest strands (FNS) for simulated data at input powers of 4 dBm (black, highest), 7 dBm (red, second highest), 9 dBm (green, second lowest), and 14 dBm (blue, lowest) (a). Comparison of the percentage of FNS for experimental data (9 dBm, green circle; 14 dBm, blue square) and simulated data (9 dBm, green dotted line; 14 dBm, blue solid line) after filtering and with addition of measurement noise (b). Black triangles represent the percentage of FNS for measured photoreceiver noise. Calculations were made on 300 000 data points.

there is a distinct transition from a noisy high-dimensional system to lower-dimensional dynamics as the input power increases and the dynamical system filters away noise from the Stokes wave.

V. CONCLUSIONS

In conclusion, although SBS is noise initiated, the decreasing dimension of the Stokes wave dynamics becomes evident with increasing input power. Nonlinear time-series analysis techniques allow us to investigate the complex dynamics of a spatiotemporal system containing stochastic elements that become less significant with increasing input power: the DFA shows a shift from Brownian motion dynamics to a system with memory, the phase analysis shows increased noise filtering, and the FNS algorithm clearly displays a decreasing dimensionality with increasing pump power. We have shown a transition from noisy high-dimensional behavior towards a lower-dimensional system dynamics through several measures with excellent agreement between experimental data and

simulations, strengthening our confidence in both the numerical model and experimental results. Physically this transition characterizes the shift from thermal phonon excitation of spontaneous Brillouin scattering, to the electrostriction-driven process of SBS. We have provided details on this shift that were previously unseen, and a better understanding of the characteristics of SBS could enable improvements in applications of its effects.

ACKNOWLEDGMENTS

We acknowledge many helpful discussions with Aaron M. Hagerstrom and D. A. Arroyo-Almanza gratefully acknowledges postdoctoral fellowship support from the Consejo Nacional de Ciencia y Tecnologia (CONACYT) Mexico. We would also like to thank the National Science Foundation for support through the REU program at the University of Maryland, College Park which allowed R.G.S to begin work on SBS.

-
- [1] A. L. Gaeta and R. W. Boyd, *Phys. Rev. A* **44**, 3205 (1991).
 [2] G. P. Agrawal, *Nonlinear Fiber Optics*, 2nd ed. (Academic Press, San Diego, 1995), Chap. 9.
 [3] R. W. Boyd, *Nonlinear Optics*, 2nd ed. (Academic Press, San Diego, 2008), Chap. 9.
 [4] D. Cotter, *Electron. Lett.* **18**, 495 (1982).
 [5] Y. Aoki, K. Tajima, and I. Mito, *Opt. Quantum Electron.* **19**, 141 (1987).
 [6] S. Mauger, L. Berge, and S. Skupin, *Phys. Rev. A* **83**, 063829 (2011).
 [7] H. Xiao-Yang, C. Wei, T. Xiao-Bo, and M. Zhou, *Chin. Phys. B* **23**, 124208 (2014).
 [8] M. Grech, G. Riazuelo, D. Pesme, S. Weber, and V. T. Tikhonchuk, *Phys. Rev. Lett.* **102**, 155001 (2009).
 [9] P. Loiseau, O. Morice, D. Teychenne, M. Casanova, S. Huller, and D. Pesme, *Phys. Rev. Lett.* **97**, 205001 (2006).
 [10] C. Rousseaux, L. Gremillet, M. Casanova, P. Loiseau, M. R. LeGloahec, S. D. Baton, F. Amiranoff, J. C. Adam, and A. Heron, *Phys. Rev. Lett.* **97**, 015001 (2006).
 [11] P. Neumayer, R. L. Berger, L. Divol, D. H. Froula, R. A. London, B. J. MacGowan, N. B. Meezan, J. S. Ross, C. Sorce, L. J. Suter, and S. H. Glenzer, *Phys. Rev. Lett.* **100**, 105001 (2008).
 [12] H. Shin, W. Qiu, R. Jarecki, J. A. Cox, R. H. Olsson III, A. Starbuck, Z. Wang, and P. T. Rakich, *Nat. Commun.* **4**, 1944 (2013).
 [13] R. Pant, C. G. Poulton, D.-Y. Choi, H. Mcfarlane, S. Hile, E. Li, L. Thevenaz, B. Luther-Davies, S. J. Madden, and B. J. Eggleton, *Opt. Express* **19**, 8285 (2011).

- [14] C. G. Poulton, R. Pant, A. Byrnes, S. Fan, M. J. Steel, and B. J. Eggleton, *Opt. Express* **20**, 21235 (2012).
- [15] A. Byrnes, R. Pant, E. Li, D. Choi, C. G. Poulton, S. Fan, S. Madden, B. Luther-Davies, and B. J. Eggleton, *Opt. Express* **20**, 18836 (2012).
- [16] P. T. Rakich, C. Reinke, R. Camacho, P. Davids, and Z. Wang, *Phys. Rev. X* **2**, 011008 (2012).
- [17] X. Guo, W. Hasi, Z. Zhong, C. Jin, D. Lin, W. He, and Z. Lu, *Laser Particle Beams* **30**, 525 (2012).
- [18] P. Dainese, P. S. J. Russell, N. Joly, J. C. Knight, G. S. Wiederhecker, H. L. Fragnito, V. Laude, and A. Khelif, *Nat. Phys.* **2**, 388 (2006).
- [19] J. Li, H. Lee, and K. J. Vahala, *Nat. Commun.* **4**, 2097 (2013).
- [20] J. Kim, M. C. Kuzyk, K. Han, H. Wang, and G. Bahl, *Nat. Phys.* **11**, 275 (2015).
- [21] V. P. Kalosha, L. Chen, and X. Bao, *Phys. Rev. A* **75**, 021802 (2007).
- [22] J. M. S. Domingo, J. Pelayo, F. Villuendas, C. D. Heras, and E. Pellejer, *IEEE Photonics Tech. Lett.* **17**, 855 (2005).
- [23] Z. Zhu, D. J. Gauthier, and R. W. Boyd, *Science* **318**, 1748 (2007).
- [24] R. W. Boyd, K. Rzazewski, and P. Narum, *Phys. Rev. A* **42**, 5514 (1990).
- [25] M. S. Mangir, J. J. Ottusch, D. C. Jones, and D. A. Rockwell, *Phys. Rev. Lett.* **68**, 1702 (1992).
- [26] R. M. Anderson and R. M. May, *Infectious Diseases of Humans: Dynamics and Control* (Oxford University Press, Oxford, 1992).
- [27] R. M. May, *Stability and Complexity in Model Ecosystems* (Princeton University Press, Princeton, 1974).
- [28] S. P. Ellner and P. Turchin, *Oikos* **111**, 620 (2005).
- [29] S. P. Ellner and J. Guckenheimer, *Dynamic Models in Biology* (Princeton University Press, Princeton, 2006).
- [30] S. Sunada, T. Harayama, P. Davis, K. Tsuzuki, K.-I. Arai, K. Yoshimura, and A. Uchida, *Chaos* **22**, 047513 (2012).
- [31] C. J. Randall and J. R. Albritton, *Phys. Rev. Lett.* **52**, 1887 (1984).
- [32] R. G. Harrison, J. S. Uppal, A. Johnstone, and J. V. Moloney, *Phys. Rev. Lett.* **65**, 167 (1990).
- [33] R. G. Harrison, P. M. Ripley, and W. Lu, *Phys. Rev. A* **49**, R24 (1994).
- [34] S. H. Lee, D.-S. Lee, and C.-M. Kim, *Opt. Express* **15**, 524 (2007).
- [35] C. Zeringue, I. Dajani, S. Naderi, G. T. Moore, and C. Robin, *Opt. Express* **20**, 21196 (2012).
- [36] C. E. Mungan, S. D. Rogers, N. Satyan, and J. O. White, *IEEE J. Quantum Electron.* **48**, 1542 (2012).
- [37] A. Melloni, M. Frasca, A. Garavaglia, A. Tonini, and M. Martinelli, *Opt. Lett.* **23**, 691 (1998).
- [38] M. O. van Deventer and A. J. Boot, *J. Lightwave Tech.* **12**, 585 (1994).
- [39] I. Velchev and W. Ubachs, *Phys. Rev. A* **71**, 043810 (2005).
- [40] V. I. Kovalev, R. G. Harrison, and J. D. Simonotto, *Phys. Rev. A* **78**, 043820 (2008).
- [41] J. Gao, Y. Ding, Z. Chen, and C. Lin, *Physica B* **442**, 1 (2014).
- [42] S. Depierreux, D. T. Michel, V. Tassin, P. Loiseau, C. Stenz, and C. Labaune, *Phys. Rev. Lett.* **103**, 115001 (2009).
- [43] E. M. Dianov, A. Ya. Karasik, A. V. Luchnikov, and A. K. Senatorov, *Sov. J. Quantum Electron.* **19**, 508 (1989).
- [44] H. Hurst, *Trans. Am. Soc. Civil Eng.* **116**, 770 (1951).
- [45] C.-K. Peng, S. V. Buldyrev, S. Havlin, M. Simons, H. E. Stanley, and A. L. Goldberger, *Phys. Rev. E* **49**, 1685 (1994).
- [46] V. A. Setty and A. S. Sharma, *Physica A* **419**, 698 (2014).
- [47] P. S. Addison, *Fractals and Chaos* (Institute of Physics Publishing, Bristol, 1997), Chap. 4.
- [48] A. Papoulis, *Probability, Random Variables, and Stochastic Processes*, 7th ed. (McGraw-Hill, New York, 1991), Chap. 7.
- [49] J. S. Lawrence Marple, *IEEE Trans. Signal Proc.* **47**, 2600 (1999).
- [50] M. Born and E. Wolf, *Principles of Optics*, 7th ed. (Cambridge University Press, Cambridge, 1999), Chap. 10.
- [51] M. B. Kennel, R. Brown, and H. D. I. Abarbanel, *Phys. Rev. A* **45**, 3403 (1992).
- [52] M. B. Kennel and H. D. I. Abarbanel, *Phys. Rev. E* **66**, 026209 (2002).